Journal of Computational Physics 229 (2010) 3402–3414

Contents lists available at ScienceDirect

Journal of Computational Physics

journal homepage: www.elsevier.com/locate/jcp

Large eddy simulation of turbulent Taylor–Couette flow using isogeometric analysis and the residual-based variational multiscale method

Y. Bazilevs *, I. Akkerman

Structural Engineering, University of California, San Diego, 9500 Gilman Drive, La Jolla, CA 92123, USA

ARTICLE INFO

Article history:
Received 14 August 2009
Accepted 10 January 2010
Available online 20 January 2010

Keywords:
Finite elements
Fluids
Weak boundary conditions
Large eddy simulation
Isogeometric analysis
Boundary layers
Navier–Stokes equations
Turbulence
NURBS
Rotating flows
Taylor–Couette flow

ABSTRACT

We present an application of the residual-based variational multiscale turbulence modeling (RBVMS) methodology to the computation of turbulent Taylor–Couette flow at high Reynolds number. We show that the RBVMS formulation globally conserves angular momentum, a feature that is felt to be important for flows dominated by rotation, and that is not shared by standard stabilized formulations of fluid flow. Weak imposition of Dirichlet boundary conditions is employed to enhance the accuracy of the RBVMS framework in the presence of thin turbulent boundary layers near solid walls. Calculation of conservative boundary forces and torques is also presented for the case of weakly enforced boundary conditions. NURBS-based isogeometric analysis is employed for the spatial discretization, and mesh refinement is performed to assess the convergence characteristics of the proposed methodology. Numerical tests show that very accurate results are obtained on relatively coarse grids. To the best of the authors' knowledge, this paper is the first to report large eddy simulation computations of this challenging test case.

1. Introduction

Rotating turbulent flows are ubiquitous in science and engineering. Their examples include atmospheric and ocean flows as well as flows about ship propellers, jet engines, and wind turbines. Rotating turbulent flows exhibit a number of features that are not present in turbulent flows without rotation. For example, in the case of a turbulent flow in a rotating pipe, mean azimuthal velocity is introduced, which makes the flow no longer unidirectional. Also, due to the effects of centrifugal forces, turbulence in the near wall region is reduced, while it is increased in the outer region (see, e.g., [42]). The presence of geometrically complex, curved no-slip walls further complicates the physics of rotating flows. However, the practical significance of turbulent rotating flows necessitates the development of accurate and efficient complex-geometry numerical procedures, that are able to predict their behavior in a variety of scenarios.

Resolving all the details of turbulent flows, especially for the cases of practical interest, is computationally prohibitive. This fact necessitates the use of turbulence modeling. In the vast majority of cases turbulence models, large eddy simulation (LES) or Reynolds-averaged Navier–Stokes (RANS), are based on adding turbulent or eddy viscosity terms to the numerical formulation to model the interaction of the small unresolved scales with large scales that can be represented on a given grid. While good success was achieved with eddy viscosity models on a variety of important turbulent flows, rotating turbulent

* Corresponding author.
E-mail address: yuri@ucsd.edu (Y. Bazilevs).

0021-9991/$ - see front matter © 2010 Elsevier Inc. All rights reserved.
doi:10.1016/j.jcp.2010.01.008

flows still remain a challenge for the eddy-viscosity-based modeling approaches. Eddy-viscosity models rely on the continuous energy transfer from low to high modes in the turbulent flow, i.e., the energy cascade. However, as explained in [47], in the presence of high flow velocity rotation rates the energy cascade is arrested, rendering most well-accepted eddy-viscosity models inconsistent in this regime.

In this work we employ the residual-based variational multiscale (RBVMS) turbulence modeling approach recently proposed in [3] (also see [12,24] for earlier references). The modeling paradigm is based on the variational multiscale theory of turbulence [21,26–28,32] and the numerical experience of stabilized methods [11,30] that are residual-based. (In this paper the term "residual" refers to the amount by which the discrete solution fails to point-wise satisfy the strong form of the Navier–Stokes equations in the spatial domain.) Stabilized methods, that have enjoyed great success in large scale, three-dimensional, complex-geometry flow simulations, may be though of as predecessors of the current approach. The RBVMS framework does not explicitly use eddy viscosities to represent the effect of the missing subgrid scales on the resolved scales. Instead, the modeling terms are derived directly from a weak (or variational) formulation of the incompressible Navier–Stokes equations.

In the presence of no-slip walls, the RBVMS framework is augmented with weakly-imposed Dirichlet boundary conditions. These were first proposed in [6] in an attempt to enhance the solution accuracy on coarse boundary layer meshes. The idea of weak enforcement of boundary conditions emanates from the work of Nitsche [41] and the developments in discontinuous Galerkin methods. Weak boundary conditions were tested on several turbulent flows in [8,9] and it was shown that the accuracy of the solution in the domain interior may be dramatically improved by allowing the flow to slip and develop turbulent features on the no-slip wall. The weak boundary condition enforcement has similarities with wall function modeling approaches, however, the origins of both methodologies are very different.

The RBVMS modeling framework is implemented using isogeometric analysis, a new computational technology proposed in [25], which is based on higher-order, smooth basis functions employed in computer-aided design and computer graphics systems. Three-dimensional Non-Uniform Rational B-Splines (NURBS) (see, e.g., [43,14]), which were the first computational technology implemented within isogeometric analysis, are employed in the computations presented here. NURBS, due to their very good approximation properties and the ability to efficiently represent many engineering shapes exactly, are very well suited for turbulent flows [3,1] that also include rotating components [7]. It should be noted that B-splines, which are progenitors of NURBS, were first successfully employed for boundary layer turbulent flow in [36–38,45].

The combination of RBVMS, weak boundary conditions, and isogeometric analysis gives rise to a powerful framework for turbulence modeling and simulation. In this work, using the proposed framework, we perform simulations of the Taylor–Couette flow, which is a flow between two concentric cylinders. The Reynolds number based on the inner cylinder wall speed and the gap between the cylinders is $Re = 8000$. This is the highest Reynolds number for which there exists a direct numerical simulation (DNS), recently performed in [15] and used here for comparison. We employ LES-size meshes and perform a grid convergence study for the Taylor–Couette problem. Earlier attempts to simulate the turbulent Taylor–Couette flow were made in [40,51], where the authors examined the stability of this flow at low, near critical Reynolds number at which the transition to turbulence occurs. In Refs. [48,50], the authors employed a stabilized finite element method to compute this problem, also at low Reynolds number. Only in recent years, several DNS computations of this flow at high Reynolds number were performed [10,16,44]. However, no LES computations or mesh convergence studies of this test case are reported in the literature to the best of the authors' knowledge. This may be attributed to the aforementioned difficulties with eddy-viscosity-based approaches for rotating turbulent flows.

This paper is organized as follows. In Section 2, the strong and weak forms of the incompressible Navier–Stokes equations are recalled, the discrete RBVMS formulation of the residual-based model is given. The formulation is then augmented with weak Dirichlet boundary condition terms. Stabilized formulation of the incompressible Navier–Stokes equation is also recalled for comparison with RBVMS. In Section 3, the derivations of the conservative boundary forces and fluxes for the discrete formulations are presented. It is shown that the RBVMS formulation conserves the global angular momentum, while stabilized formulations do not. In this section a special emphasis is placed on the extraction of torque that the fluid exerts on the cylinder walls, a quantity that we use to assess convergence under mesh refinement. In Section 4, numerical results for the turbulent Taylor–Couette flow are presented in the form of mean and fluctuating azimuthal velocity, angular momentum and torque exerted by the fluid on the cylinder walls. Accurate results on relatively coarse meshes are obtained using the RBVMS formulation in conjunction with quadratic NURBS. In Section 5, conclusions are drawn.

2. Incompressible Navier–Stokes equations and weakly-imposed Dirichlet boundary conditions

2.1. Strong and weak formulations

Let $\Omega \subset \mathbb{R}^d$, $d = 2, 3$ denote the spatial domain occupied by the fluid, and let $\Gamma = \partial\Omega$ be its boundary. The fluid is governed by the Navier–Stokes equations of incompressible flow. The strong form of initial/boundary-value problem is:

$$\mathcal{L}(\boldsymbol{u}, p) = \rho \boldsymbol{f} \quad \text{in } \Omega, \tag{1}$$

$$\nabla \cdot \boldsymbol{u} = 0 \quad \text{in } \Omega, \tag{2}$$

$$\boldsymbol{u} = \boldsymbol{g} \quad \text{on } \Gamma, \tag{3}$$

$$\boldsymbol{u}(\boldsymbol{x}, 0) = \boldsymbol{u}_0(\boldsymbol{x}) \quad \forall \boldsymbol{x} \in \Omega, \tag{4}$$

where

$$\mathcal{L}(\boldsymbol{u},p)=\rho\frac{\partial \boldsymbol{u}}{\partial t}+\rho\nabla\cdot(\boldsymbol{u}\otimes\boldsymbol{u})+\nabla p-\nabla\cdot(2\mu\nabla^s\boldsymbol{u}) \tag{5}$$

is the linear momentum Navier–Stokes operator, and

$$\nabla^s\boldsymbol{u}=\frac{1}{2}(\nabla\boldsymbol{u}+\nabla\boldsymbol{u}^T) \tag{6}$$

is the symmetric gradient of the velocity.

Eqs. (1)–(4) are the balance of linear momentum, incompressibility constraint, and boundary and initial conditions, respectively, ρ is the fluid density, $\boldsymbol{f}$ is the body force, μ is the kinematic viscosity, $\boldsymbol{u}$ is the fluid particle velocity vector, and p is the pressure. We only consider the Dirichlet problem, which imposes an additional zero-mean constraint on the pressure field ($\int_\Omega p\,d\Omega=0$). This is done to simplify the exposition and is not a limitation of the proposed methodology. Note that we can use the incompressibility constraint to obtain an alternative form of the linear momentum equation

$$\mathcal{L}_{adv}(\boldsymbol{u},p)=\rho\boldsymbol{f}\quad\text{in }\Omega, \tag{7}$$

where

$$\mathcal{L}_{adv}(\boldsymbol{u},p)=\rho\frac{\partial \boldsymbol{u}}{\partial t}+\rho\boldsymbol{u}\cdot\nabla\boldsymbol{u}+\nabla p-\mu\Delta\boldsymbol{u}, \tag{8}$$

is the so-called "advective" form of $\mathcal{L}(\boldsymbol{u},p)$.

To formulate the weak statement of the problem, we introduce $\mathcal{V}$ and $\mathcal{W}$, the trial solution and weighting function spaces, respectively. $\mathcal{V}$ and $\mathcal{W}$ are infinite-dimensional. Multiplying (1) and (2) by a test function from $\mathcal{W}$, integrating over Ω, and assuming $\boldsymbol{w}=\boldsymbol{0}$ on Γ we arrive at the weak or variational statement of the problem: Find $\{\boldsymbol{u},p\}\in\mathcal{V}$ such that $\{\boldsymbol{w},q\}\in\mathcal{W}$,

$$B(\{\boldsymbol{w},q\},\{\boldsymbol{u},p\})-(\boldsymbol{w},\boldsymbol{f})_\Omega=0, \tag{9}$$

where

$$B(\{\boldsymbol{w},q\},\{\boldsymbol{u},p\})=\left(\boldsymbol{w},\rho\frac{\partial \boldsymbol{u}}{\partial t}\right)_\Omega-(\nabla\boldsymbol{w},\rho\boldsymbol{u}\otimes\boldsymbol{u})_\Omega+(q,\nabla\cdot\boldsymbol{u})_\Omega-(\nabla\cdot\boldsymbol{w},p)_\Omega+(\nabla^s\boldsymbol{w},2\mu\nabla^s\boldsymbol{u})_\Omega, \tag{10}$$

and $(\cdot,\cdot)_\Omega$ denotes the $L^2(\Omega)$ inner product. Provided the velocity and pressure solutions are sufficiently smooth, the strong and weak statements are equivalent. The weak statement of the problem given in Eq. (9) is the point of departure for the residual-based variational multiscale (RBVMS) turbulence model to be summarized in the sequel.

2.2. Residual-based variational multiscale (RBVMS) turbulence modeling

The residual-based variational multiscale modeling of turbulence emanates from the theory of variational multiscale methods [3]. The trial solution and weighting function spaces are split into subspaces that contain coarse and fine scales. This is accomplished by a multiscale direct-sum decomposition

$$\mathcal{V}=\mathcal{V}^h\oplus\mathcal{V}', \tag{11}$$

$$\mathcal{W}=\mathcal{W}^h\oplus\mathcal{W}'. \tag{12}$$

In the above, $\mathcal{V}^h$ and $\mathcal{W}^h$ are the spaces of coarse scales. These are finite-dimensional function spaces associated with a numerical discretization (e.g., finite elements, NURBS, Fourier series). On the other hand, $\mathcal{V}'$ and $\mathcal{W}'$, spaces of fine scales, are infinite-dimensional and represent information that is not present in the discretization (e.g., the Fourier modes beyond cut-off). It is precisely for this reason that they are called subgrid scales. Eqs. (11) and (12) imply that every member of $\mathcal{V}$ and $\mathcal{W}$ can be uniquely written as

$$\{\boldsymbol{u},p\}=\{\boldsymbol{u}^h,p^h\}+\{\boldsymbol{u}',p'\}, \tag{13}$$

$$\{\boldsymbol{w},q\}=\{\boldsymbol{w}^h,q^h\}+\{\boldsymbol{w}',q'\}. \tag{14}$$

Substituting (13) into (9) and choosing $\{\boldsymbol{w},q\}=\{\boldsymbol{w}^h,q^h\}$ (recall that (9) holds for all possible $\{\boldsymbol{w},q\}\in\mathcal{W}$) yields

$$B(\{\boldsymbol{w}^h,q^h\},\{\boldsymbol{u}^h,p^h\}+\{\boldsymbol{u}',p'\})-(\boldsymbol{w}^h,\rho\boldsymbol{f})_\Omega=0,\quad\forall\{\boldsymbol{w}^h,q^h\}\in\mathcal{W}^h. \tag{15}$$

Because $\{\boldsymbol{w}^h,q^h\}$ are in a finite-dimensional space, (15) leads to a finite-dimensional system of equations for which the large scales $\{\boldsymbol{u}^h,p^h\}$ are the unknowns. The variational statement (15) gives a precise way in which the large scale equations depend on the fine-scale fields.

The fine scales $\{\boldsymbol{u}',p'\}$ are not given and their effect in the coarse-scale equations must be modeled. The fine scale equations, obtained by choosing $\{\boldsymbol{w},q\}=\{\boldsymbol{w}',q'\}$ in (9), reveal that the fine scales are driven by the residual of the coarse scales (see [3] for an elaboration and a detailed derivation that we do not repeat here).

The following simple fine-scale model, which makes the fine scales proportional to the coarse-scale residuals of the Navier–Stokes equations, was proposed in [3] (also see [12,24] for earlier references):

$$\boldsymbol{u}' = -\tau_M \boldsymbol{r}_M(\{\boldsymbol{u}^h, p^h\}), \tag{16}$$

$$p' = -\tau_C r_C(\boldsymbol{u}^h), \tag{17}$$

where $\boldsymbol{r}_M(\{\boldsymbol{u}^h, p^h\})$ and $r_C(\boldsymbol{u}^h)$ are the coarse-scale residuals of the linear momentum equation and incompressibility constraint, namely,

$$\boldsymbol{r}_M(\boldsymbol{u}, p) = \mathcal{L}_{adv}(\boldsymbol{u}, p) - \rho \boldsymbol{f}, \tag{18}$$

$$r_C(\boldsymbol{u}) = \nabla \cdot \boldsymbol{u}. \tag{19}$$

where τ_M and τ_C are strictly positive scalar functions of the mesh (element size and shape, and the polynomial order of the discretization), time step size, and flow velocity. Their exact definitions are given in [3], and are summarized in the Appendix. The proposed model for the fine scales (16)–(18) satisfies the following consistency conditions: (1) The fine scales are identically zero if the discrete solution satisfies the Navier–Stokes equations point-wise; (2) The fine scales also go to zero in the limit of infinite resolution in both space and time. The former condition is a direct consequence of the residual-based definition of the small scales, while the latter is tied to the design of stabilization parameters.

Using integration-by-parts on the fine-scale terms in (15) and substituting expressions (16) and (17) for the fine scales leads to the following discrete variational formulation: Find $\{\boldsymbol{u}^h, p^h\} \in \mathcal{V}^h$, $\boldsymbol{u}^h = \boldsymbol{g}$ on Γ, such that $\forall \{\boldsymbol{w}^h, q^h\} \in \mathcal{V}^h$, $\boldsymbol{w}^h = \boldsymbol{0}$ on Γ,

$$B(\{\boldsymbol{w}^h, q^h\}, \{\boldsymbol{u}^h, p^h\}) + B_{mod}(\{\boldsymbol{w}^h, q^h\}, \{\boldsymbol{u}^h, p^h\}) - (\boldsymbol{w}^h, \rho \boldsymbol{f})_\Omega = 0, \tag{20}$$

where the modeled subgrid-scale terms in B_{mod} are

$$\begin{aligned} B_{mod}(\{\boldsymbol{w}, q\}, \{\boldsymbol{u}, p\}) = {} & (\{\rho \boldsymbol{u} \cdot \nabla \boldsymbol{w} + \nabla q\}, \tau_M \boldsymbol{r}_M(\boldsymbol{u}, p))_\Omega + (\nabla \cdot \boldsymbol{w}, \tau_C r_C(\boldsymbol{u}))_\Omega + (\{\rho \boldsymbol{u} \cdot (\nabla \boldsymbol{w})^T\}, \tau_M \boldsymbol{r}_M(\boldsymbol{u}, p))_\Omega \\ & - (\nabla \boldsymbol{w}, \rho \tau_M \boldsymbol{r}_M(\boldsymbol{u}, p) \otimes \tau_M \boldsymbol{r}_M(\boldsymbol{u}, p))_\Omega. \end{aligned} \tag{21}$$

The functions τ_M and τ_C in the above equations originate from stabilized finite element methods for fluid dynamics (see, e.g., [11,19,30,31,49]) and are referred to as stabilization parameters. They were designed and studied extensively in the context of stabilized finite element formulations of linear model problems of direct relevance to fluid mechanics. These model problems include advection–diffusion and Stokes equations. The design of τ_M and τ_C is such that optimal convergence with respect to the mesh size and polynomial order of discretization is attained for these cases (see, e.g., [30] and references therein). Furthermore, enhanced stability for advection dominated flows and the ability to conveniently employ the same basis functions for velocity and pressure variables for incompressible flow are some of the attractive outcomes of this methodology. More recently, the fine-scale models of the form given in Eqs. (16) and (17) were derived in the context of the variational multiscale methods [22,23]. Here τ_M and τ_C are interpreted as the appropriate averages of the small-scale Green's function, a key mathematical object in the theory of variational multiscale methods (see [29] for an elaboration).

To compare the formulation given by (20) and (21) with a well-know stabilized formulation of the Navier–Stokes equations of incompressible flow, we formulate the latter as: Find $\{\boldsymbol{u}^h, p^h\} \in \mathcal{V}^h$, $\boldsymbol{u}^h = \boldsymbol{g}$ on Γ, such that $\forall \{\boldsymbol{w}^h, q^h\} \in \mathcal{V}^h$, $\boldsymbol{w}^h = \boldsymbol{0}$ on Γ,

$$B(\{\boldsymbol{w}^h, q^h\}, \{\boldsymbol{u}^h, p^h\}) + B_{stab}(\{\boldsymbol{w}^h, q^h\}, \{\boldsymbol{u}^h, p^h\}) - (\boldsymbol{w}^h, \rho \boldsymbol{f})_\Omega = 0, \tag{22}$$

where the stabilization terms in B_{stab} are

$$B_{stab}(\{\boldsymbol{w}, q\}, \{\boldsymbol{u}, p\}) = (\{\rho \boldsymbol{u} \cdot \nabla \boldsymbol{w} + \nabla q\}, \tau_M \boldsymbol{r}_M(\boldsymbol{u}, p))_\Omega + (\nabla \cdot \boldsymbol{w}, \tau_C r_C(\boldsymbol{u}))_\Omega. \tag{23}$$

The difference between the stabilized and RBVMS formulations comes from the last two terms in the definition of B_{mod} in (21). We will see in the sequel that precisely because of this seemingly small difference RBVMS globally conserves angular momentum, while stabilized formulation (22) does not. The authors feel that global angular momentum conservation is important, especially for turbulent flows dominated by rotation.

2.3. Weak Dirichlet boundary conditions

In the presence of solid no-slip walls, the variational multiscale formulation (20) may be augmented with weakly-imposed Dirichlet boundary conditions. Weak boundary conditions, which are based on Nitsche's approach [41] and concepts from Discontinuous Galerkin methods, were proposed in [6] for the advection diffusion and incompressible Navier–Stokes equations, and further enhanced in [8,9]. For this case the RBVMS formulation (20) becomes: Find $\{\boldsymbol{u}^h, p^h\} \in \mathcal{V}^h$, such that $\forall \{\boldsymbol{w}^h, q^h\} \in \mathcal{V}^h$,

$$B(\{\boldsymbol{w}^h, q^h\}, \{\boldsymbol{u}^h, p^h\}) + B_{mod}(\{\boldsymbol{w}^h, q^h\}, \{\boldsymbol{u}^h, p^h\}) + B_{wbc}(\{\boldsymbol{w}^h, q^h\}, \{\boldsymbol{u}^h, p^h\}) - (\boldsymbol{w}^h, \rho \boldsymbol{f})_\Omega = 0, \tag{24}$$

where the weak boundary condition terms in B_{wbc} are

$$B_{wbc}(\{\boldsymbol{w},q\},\{\boldsymbol{u},p\}) = (\boldsymbol{w},\rho(\boldsymbol{u}\cdot\boldsymbol{n})\boldsymbol{u}+p\boldsymbol{n}-2\mu\nabla^s\boldsymbol{u}\cdot\boldsymbol{n})_\Gamma + (2\mu\nabla^s\boldsymbol{w}\cdot\boldsymbol{n}-q\boldsymbol{n},\boldsymbol{u}-\boldsymbol{g})_\Gamma - (\rho(\boldsymbol{u}\cdot\boldsymbol{n})\boldsymbol{w},\boldsymbol{u}-\boldsymbol{g})_{\Gamma_{in}} + (\boldsymbol{w},\rho\tau_B(\boldsymbol{u}-\boldsymbol{g}))_\Gamma = 0, \tag{25}$$

The terms on the first line on the right-hand-side of (25) ensure consistency of the formulation. This means equality (24) holds when $\{\boldsymbol{u}^h,p^h\}$ are replaced with the exact solution of the Navier–Stokes equations. The terms on the second and third lines of (25) ensure adjoint consistency. Adjoint consistency means equality (24) holds when $\{\boldsymbol{w}^h,q^h\}$ are replaced with the exact solution of the adjoint Navier–Stokes problem. Adjoint consistency leads to optimal convergence in lower order norms (see, e.g., [2]) and is seen as an important ingredient in the formulation. Finally, the last terms in (25) guarantee the stability of the discrete formulation provided the penalty parameter τ_B is appropriately defined. The penalty parameter was introduced in [6] for a purely numerical version of weak boundary condition enforcement, and its definition was further refined on the basis of the "law-of-the-wall" in [8]. See Appendix for the details of τ_B definition.

The discrete formulation (24) will be used to compute the Taylor–Couette flow in this paper. Note that no constraints on the solution and weighting spaces at the domain boundary are imposed in the above formulation. The desired boundary conditions are enforced as Euler–Lagrange conditions in a weak sense due to the additional boundary terms B_{wbc} in (24).

3. Conservative forces and moments for weakly-imposed boundary conditions

Forces and moments are often the quantities of interest in engineering simulation. They depend on stresses, which are derived quantities in the simulation, and, as a result, have lower accuracy than the primary variables. Improved accuracy of forces and moments may be attained by defining them using conservation arguments, which we do in this section.

We begin with the RBVMS formulation (24) and introduce a special weighting function $\{\boldsymbol{w}^h,q^h\}_i = \{\boldsymbol{e}_i,0\}$, where $\boldsymbol{e}_i$ is the ith Cartesian basis vector. We use the index i to indicate that there are d separate test functions, one for each Cartesian direction. This choice of the test function is permissible, because global constants are in our discrete space. The following equation is obtained,

$$\left(\boldsymbol{e}_i,\rho\frac{\partial\boldsymbol{u}^h}{\partial t}-\rho\boldsymbol{f}\right)+B_{wbc}(\{\boldsymbol{e}_i,0\},\{\boldsymbol{u}^h,p^h\})=0, \tag{26}$$

which may be re-written as

$$\int_\Omega \rho\frac{\partial u_i^h}{\partial t}-\rho f_i\,d\Omega = -B_{wbc}(\{\boldsymbol{e}_i,0\},\{\boldsymbol{u}^h,p^h\}), \tag{27}$$

where u_i^h and f_i are the components of the discrete velocity and body force vectors, respectively, and the summation on repeated indices is implied. The right-hand-side of the above Eq. (27) may be interpreted as the global boundary force or flux that restores the balance of linear momentum. The components of the conservative force vector, denoted by h_i, are obtained directly from the definition of B_{wbc} as

$$h_i = -B_{wbc}(\{\boldsymbol{e}_i,0\},\{\boldsymbol{u}^h,p^h\}) = -\int_\Gamma p^h n_i-\mu\left(\frac{\partial u_i^h}{\partial x_j}+\frac{\partial u_j^h}{\partial x_i}\right)n_j\,d\Gamma-\int_{\Gamma_{in}}\rho(u_j^h n_j)g_i\,d\Gamma-\int_{\Gamma_{out}}\rho(u_j^h n_j)u_i^h\,d\Gamma-\int_\Gamma\rho\tau_B(u_i^h-g_i)d\Gamma, \tag{28}$$

where Γ_{in} and Γ_{out} are the inflow and outflow parts of the boundary, respectively, defined in a usual way. Note that the global force vector is comprised of terms that come from the direct evaluation of the boundary force vector as well as terms that account for the errors in the satisfaction of the essential boundary conditions. The treatment of inflow and outflow boundaries are likewise different. Also note that the fine-scale terms do not influence the global balance of linear momentum, that is, $B_{mod}(\{\boldsymbol{e}_i,0\},\{\boldsymbol{u}^h,p^h\})=0_i$, which means that the fine scales enter the discrete formulation in a conservative manner with respect to global linear momentum. The same holds true for the stabilized formulation (22). A simple calculation shows that $B_{stab}(\{\boldsymbol{e}_i,0\},\{\boldsymbol{u}^h,p^h\})=0_i$, which implies that the stabilization terms do not influence global momentum conservation.

We now consider another choice of the weighting function. We set $\{\boldsymbol{w}^h,q^h\}_i=\{\varepsilon_{ijk}r_j\boldsymbol{e}_k,0\}$, where ε_{ijk} are the components of the alternator tensor, r_j's are the components of the radius vector $\boldsymbol{r}=\boldsymbol{x}-\boldsymbol{x}_0$, and $\boldsymbol{x}_0$ is a fixed location in $\mathbb{R}^d$. This is a permissible choice for a test function because global linear polynomials are in our discrete space, a consequence of the isoparametric concept employed in both finite elements and isogeometric analysis. Introducing this weighting function in Eq. (24), gives

$$0_i = B(\{\varepsilon_{ijk}r_j\boldsymbol{e}_k,0\},\{\boldsymbol{u}^h,p^h\})+B_{mod}(\{\varepsilon_{ijk}r_j\boldsymbol{e}_k,0\},\{\boldsymbol{u}^h,p^h\})+B_{wbc}(\{\varepsilon_{ijk}r_j\boldsymbol{e}_k,0\},\{\boldsymbol{u}^h,p^h\})-(\boldsymbol{w}^h,\rho\boldsymbol{f})_\Omega. \tag{29}$$

To examine the individual terms on the right-hand-side on the above equation, we first compute the spatial gradient of the proposed test function as follows,

$$\nabla\varepsilon_{ijk}r_j\boldsymbol{e}_k=\frac{\partial\varepsilon_{ijk}r_j}{\partial x_l}\boldsymbol{e}_k\otimes\boldsymbol{e}_l=\varepsilon_{ijk}\delta_{jl}\boldsymbol{e}_l\otimes\boldsymbol{e}_k=\varepsilon_{ijk}\boldsymbol{e}_j\otimes\boldsymbol{e}_k. \tag{30}$$

Due to the properties of the alternator ε_{ijk}, the above gradient is a skew-symmetric tensor, which is orthogonal to any symmetric tensor. This observation leads to the following simplifications,

$$B(\{\varepsilon_{ijk} r_j \boldsymbol{e}_k, 0\}, \{\boldsymbol{u}^h, p^h\}) - (\boldsymbol{w}^h, \rho \boldsymbol{f})_\Omega = \left(\varepsilon_{ijk} r_j \boldsymbol{e}_k, \rho \frac{\partial \boldsymbol{u}^h}{\partial t} - \rho \boldsymbol{f}\right), \tag{31}$$

where the only terms that survive are the fluid acceleration and body force. Analysis of the modeling terms yields

$$B_{mod}(\{\varepsilon_{ijk} r_j \boldsymbol{e}_k, 0\}, \{\boldsymbol{u}^h, p^h\}) = (\varepsilon_{ijk} \boldsymbol{e}_j \otimes \boldsymbol{e}_k, \rho \tau_M (\boldsymbol{r}_M \otimes \boldsymbol{u}^h + \boldsymbol{u}^h \otimes \boldsymbol{r}_M + \tau_M \boldsymbol{r}_M \otimes \boldsymbol{r}_M))_\Omega = 0_i, \tag{32}$$

where the last equality holds because the tensor that includes the residual terms is symmetric.

Combining Eqs. (29)–(31), we obtain

$$\left(\varepsilon_{ijk} r_j \boldsymbol{e}_k, \rho \frac{\partial \boldsymbol{u}^h}{\partial t} - \rho \boldsymbol{f}\right) = -B_{wbc}(\{\varepsilon_{ijk} r_j \boldsymbol{e}_k, 0\}, \{\boldsymbol{u}^h, p^h\}). \tag{33}$$

The right-hand-side of (33) may be interpreted as defining the components of the boundary torque that ensures a global balance of angular momentum. The cartesian components of the conservative torque vector denoted by t_i are now given by

$$\begin{aligned} t_i &= -B_{wbc}(\{\varepsilon_{ijk} r_j \boldsymbol{e}_k\}, \{\boldsymbol{u}^h, p^h\}) \\ &= -\varepsilon_{ijk}\left(\int_\Gamma r_j p^h n_k - r_j \mu \left(\frac{\partial u_k^h}{\partial x_l} + \frac{\partial u_l^h}{\partial x_k}\right) n_l \, d\Gamma - \int_{\Gamma_{in}} r_j \rho (u_l^h n_l) g_k \, d\Gamma - \int_{\Gamma_{out}} r_j \rho (u_l^h n_l) u_k^h \, d\Gamma - \int_\Gamma r_j \rho \tau_B (u_k^h - g_k) d\Gamma\right). \end{aligned} \tag{34}$$

As in the case of the conservative force, the above expression for the conservative torque contains terms that arise due to the lack of exact satisfaction of Dirichlet boundary conditions. The treatment of inflow and outflow parts of the boundary are like wise different.

Remark. In the case of the stabilized method given by Eq. (22), we compute

$$B_{stab}(\{\varepsilon_{ijk} r_j \boldsymbol{e}_k, 0\}, \{\boldsymbol{u}^h, p^h\}) = (\varepsilon_{ijk} \boldsymbol{e}_j \otimes \boldsymbol{e}_k, \rho \tau_M \boldsymbol{r}_M \otimes \boldsymbol{u}^h)_\Omega \neq 0_i. \tag{35}$$

Comparing Eqs. (32) and (35) we find that the RBVMS formulation globally conserves angular momentum, while the stabilized formulation does not.

4. Turbulent Taylor–Couette flow at $Re = 8000$

We simulate the turbulent Taylor–Couette flow, which is a flow between two concentric cylinders. This is a very good test case for verification and validation of numerical formulations for turbulent fluid flow for the following reasons: (1) The flow exhibits several complex features, such as rotation, curved walls, and highly complex time-dependent evolution of the velocity and pressure fields, all of which are a challenging to compute; (2) Much is known about this problem experimentally (see, e.g., [39]), and, very recently, several DNS simulations of this test case were computed [10,44,16], all of which produce high-fidelity data that may be used for comparison purposes.

The flow domain is the volume enclosed between two concentric cylinders. The inner cylinder is assumed to rotate at constant angular velocity, while the outer cylinder in stationary. The problem setup and dimensions are shown in Fig. 1. The problem Reynolds number, $Re = U_\theta (R_1 - R_0)\rho/\mu = 8000$, where $\rho = 1$ is the fluid density, $\mu = 1/8000$ is the dynamic viscosity, $R_0 = 1$ and $R_1 = 2$ are the cylinder inner and outer radii, respectively, and $U_\theta = 1$ is the flow speed at the inner cylinder wall. Periodic boundary conditions are imposed in the axial direction, and no-slip boundary conditions are applied at the cylinder surfaces.

In the remainder of the section we describe our spatial and temporal discretization and present numerical results for the Taylor–Couette test case.

4.1. Spatial discretization: isogeometric analysis

To discretize the semi-linear form (24) in space, we use isogeometric analysis, a new computational technology that was recently introduced in [25]. Isogeometric analysis is based on technologies in computational geometry and computer-aided design and can be thought of as a generalization of the finite element method. Isogeometric analysis and FEM have many features in common, such as an underlying variational framework, compactly supported basis functions and geometric flexibility. However, isogeometric analysis has several advantages over FEA and offers new possibilities that do not exist in finite elements: precise and efficient modeling of complex geometrical configurations and smooth basis functions with degree of continuity beyond C^0. Analogs of finite element h- and p-mesh refinements procedures exist in isogeometric analysis. However, a unique feature of isogeometric analysis not shared by standard finite elements is the so-called k-refinement, in which the order of the basis functions is elevated together with continuity. Smooth basis functions that are C^1- or higher-continuous can be directly employed to discretize higher-order differential operators (see, e.g., [20] for a recent application of isogeometric analysis to phase field modeling of phase separation governed by the Cahn–Hilliard equation.) Furthermore, using functions of higher continuity in situations when C^0-continuous discretizations are sufficient was shown to be beneficial for

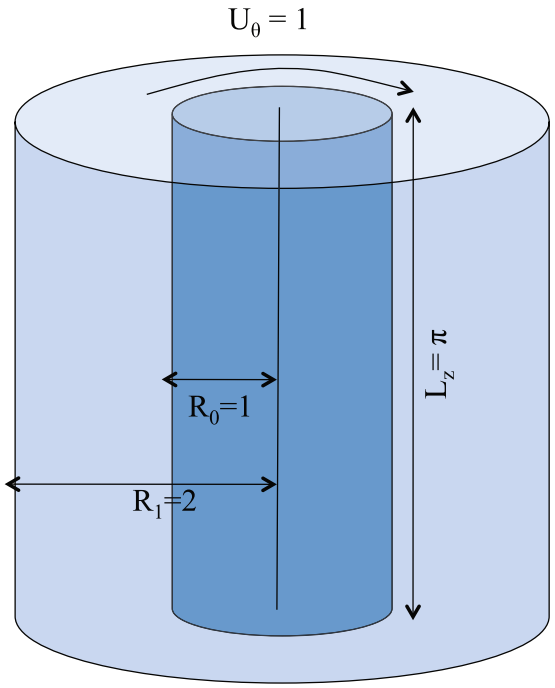

Fig. 1. Turbulent Taylor–Couette flow: Problem setup.

accuracy and robustness of the computational results in numerous situations. A particularly noteworthy increase in accuracy due to the use of higher-continuity functions was observed in turbulent flow computations in [1].

We make use of isogeomeric analysis based on NURBS (non-uniform rational B-splines) [14,43]. NURBS are built from B-splines through a projective transformation [18]. They are a standard basis function technology used in computer-aided design and computer graphics, and the first and most widely employed computational technology in isogeometric analysis. NURBS have superior approximation power than standard, low-order finite elements [5,17]. Quadratic and higher-order NURBS can represent all conic sections exactly, which include circular and cylindrical shapes. This fact makes them particularly attractive for computing flows that involve rotating components, which may be embedded in the stationary flow domain without geometrical error [7].

We use quadratic NURBS in the computations. We perform our simulations using a sequence of h-refined meshes to assess the convergence properties of the proposed numerical methodology. The continuity of the basis functions is kept at the C^1 level at mesh knots, which is maximal continuity of the basis that is achievable for a quadratic discretization. We note that at each level of refinement, quadratic NURBS capture the problem geometry exactly. This would not be the case for linear finite elements, which approximate the circular geometry using flat polynomial facets. The coarsest mesh is comprised of $32 \times 8 \times 16$ elements in the azimuthal, radial, and axial directions. With each h-refinement step we double the number of elements in each parametric direction until we achieve our finest discretization of $128 \times 32 \times 64$ elements. A uniform mesh is used in the azimuthal and axial directions. In the radial direction, the meshes are obtained by distributing the knots according to a hyperbolic tangent function to better capture the boundary layer turbulence. It should be noted that the number of basis functions in the periodic directions equals to the number of elements in these directions. In the radial direction, due to open knot vector construction (see, e.g., [25]), the number of basis functions n_b is computed as $n_b = n_{el} + p$, where n_{el} is the number of elements and p is the polynomial order of the NURBS basis.

4.2. Numerical results

The flow is advanced in time using the generalized-α method [4,13,33] and the nonlinear equations are solved using an inexact Newton–Krylov approach with the assembled element-by-element preconditioner (see [3] for implementation details and [9] for the linear equation preconditioning strategy). The time step was set to 0.025 and four Newton iterations were used in each time step.

Flow statistics are presented in the form of ensemble-averaged mean azimuthal velocity, angular momentum, and azimuthal velocity fluctuations, all as functions of the radial coordinate. Velocity data are collected at mesh knots, rotated to the cylindrical coordinate system (the simulations are done in cartesian coordinates), and averaged over azimuthal and axial directions as well as time. In all cases, the initial azimuthal velocity profile was set to $u_\theta = 0.5$ in the domain interior and $u_\theta = 1$ and $u_\theta = 0$ at the cylinder inner and outer walls, respectively. All other velocity components as well as pressure were

set to zero in the beginning of the computation. The flow was advanced in time until the solution reached a statistically-stationary state. At this stage, the flow data were collected for the period of 250 non-dimensional time units. We compare our results to the DNS of Dong [15], who computed this test case using Fourier series in the axial direction and spectral finite elements in the remaining directions. For an overview of spectral finite elements applied to computational fluid dynamics and turbulence see, for example, [35].

Fig. 2 shows mean azimuthal velocity results. The coarsest mesh gives a reasonably accurate result, especially considering how few degrees of freedom are utilized. The accuracy of results improves with the next level of refinement, most notably in the boundary layer, however, very minor deviation from the DNS result in the core of the domain is still present. At the finest level of discretization, quadratic NURBS produce results that are practically indistinguishable from the DNS.

Fig. 3 shows convergence of the mean angular momentum that is obtained by multiplying the mean angular velocity with the fluid density and the radial coordinate. The figure illustrates that in the core of the flow the mean angular momentum is essentially constant and equal to $0.5\rho R_0 U_0$, a phenomenon observed experimentally and also discussed in [15].

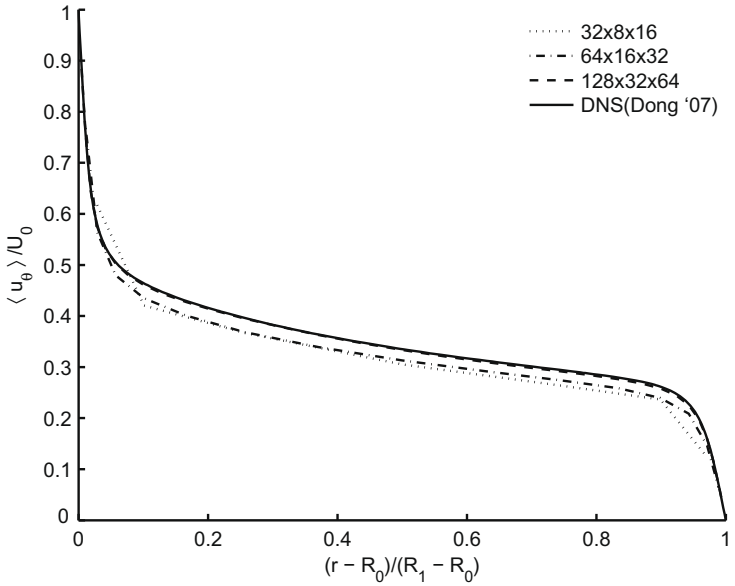

Fig. 2. Turbulent Taylor–Couette flow: Mean azimuthal velocity.

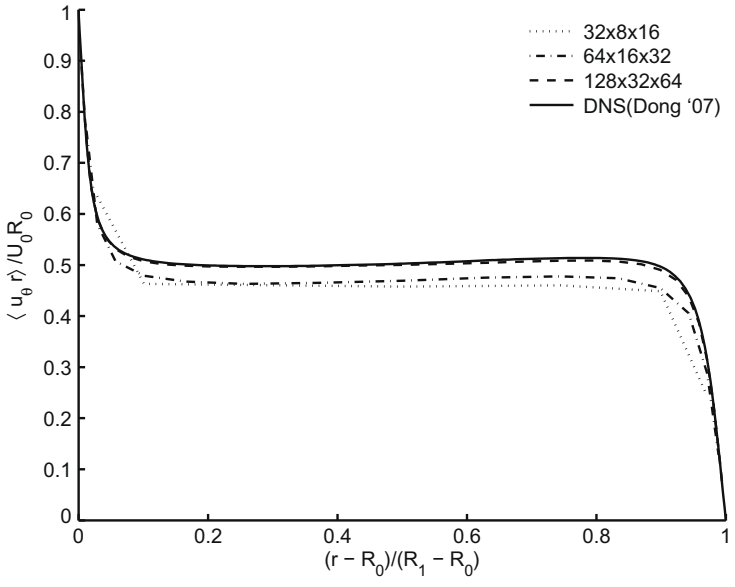

Fig. 3. Turbulent Taylor–Couette flow: Mean angular momentum.

Fig. 4 shows root-mean-square (RMS) of the azimuthal velocity fluctuations. It is generally accepted that this second-order statistic is harder to converge under mesh refinement than the mean flow. On the coarsest mesh, some deviation from the DNS is present. The quality of the velocity fluctuation results improves significantly after the first mesh refinement. At the finest mesh level, the fluctuations are in very close agreement with the DNS (the two curves practically coincide), except for a slight overshoot near the inner cylinder wall at the location that corresponds to the peak of the azimuthal velocity fluctuations.

Fig. 5 shows convergence of the magnitude of the torque exerted by the fluid on the inner cylinder wall. The torque is computed according to the conservative definition given in Eq. (34). The torque data is presented in the form of a torque coefficient C_T that is defined as the following non-dimensional quantity

$$C_T = -\frac{\langle t_3 \rangle}{0.5\pi\rho U_0^2 R_0^2 L_z}. \tag{36}$$

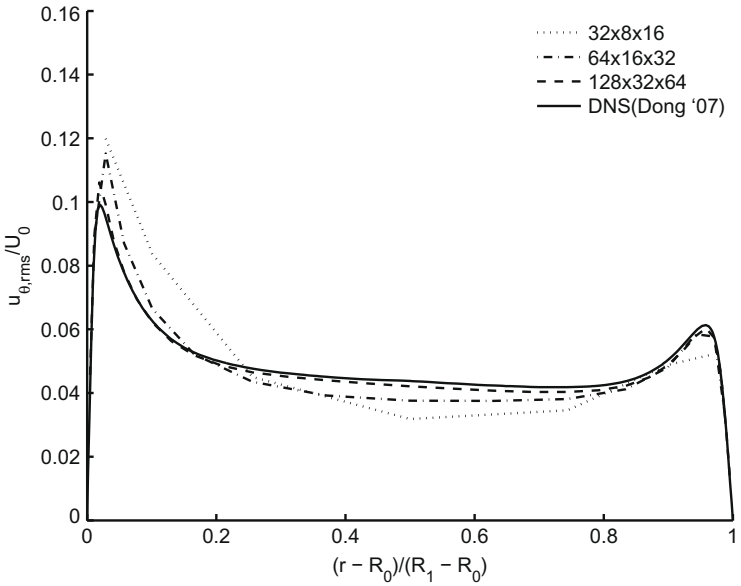

Fig. 4. Turbulent Taylor–Couette flow: Root-mean-square of azimuthal velocity fluctuations.

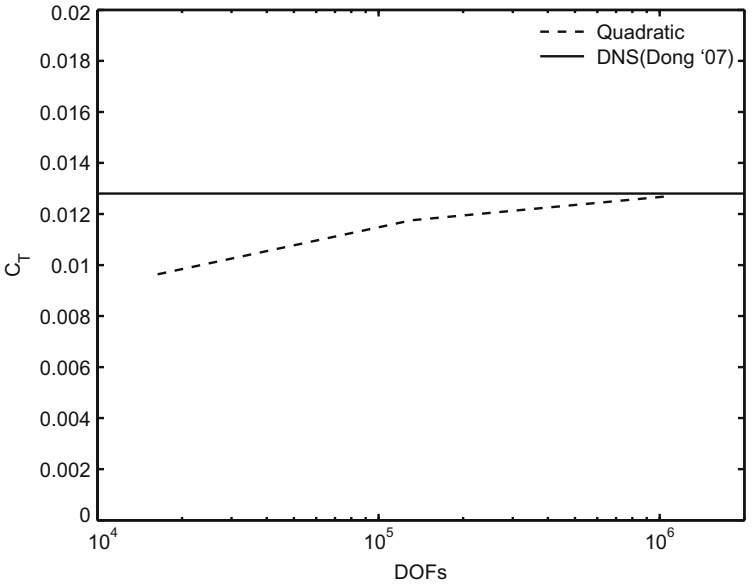

Fig. 5. Turbulent Taylor–Couette flow: Convergence of the torque.

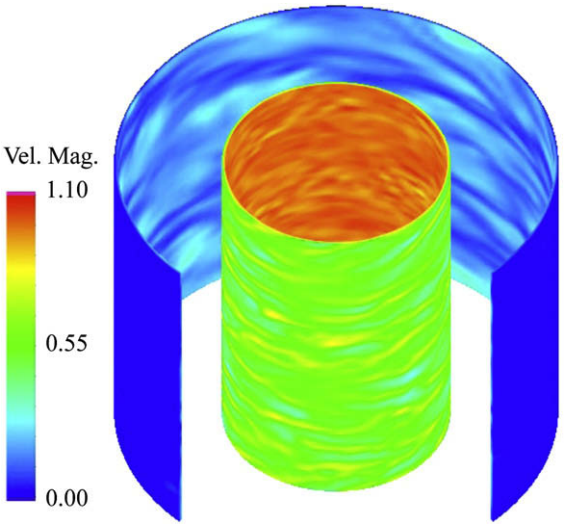

Fig. 6. Turbulent Taylor–Couette flow: Contours of the flow speed at and near the inner and outer walls.

In (36), t_3 is the axial component of the torque vector from Eq. (34) and $\langle\cdot\rangle$ denotes time average. The value of C_T that corresponds to Test Case G from the DNS calculation of Dong [15] is taken as a reference value. Test case G in the reference corresponds to the finest simulation with the identical problem setup to that reported in this paper. Torque coefficient data are plotted as a function of the number of degrees of freedom employed in the simulations (DOF). DOF is computed as the total number of basis functions in the discretization times four degrees of freedom per basis function (three velocities and a pressure). The torque coefficient converges to the reference value. Our finest mesh gives an error that is less than 1% of that reported in [15].

Fig. 6 shows isosurfaces of the instantaneous flow velocity magnitude on and near the cylinder walls for the finest quadratic mesh simulation. Note the presence of fine-grained local variations of the flow speed at the inner cylinder wall that is due to weak enforcement of boundary conditions. Also note that the velocity magnitude drops rapidly within the first element at the wall, and fast and slow streaks are formed in the boundary layer. Near the outer wall the turbulent features of the flow are significantly more coarse-grained and virtually no turbulent features are present at the outer cylinder wall. This is because of the local Reynolds number of the flow near the outer wall is lower.

5. Conclusions

We presented the application of the RBVMS methodology in conjunction with the weak enforcement of Dirichlet boundary condition to the LES computation of high-Reynolds-number turbulent Taylor–Couette flow. To the best of the authors' knowledge, no LES efforts were reported for this problem to date. Isogeometric analysis using C^1-continuous quadratic NURBS was employed in the simulations and h-refinement was performed to assess the accuracy of the proposed approach. We note that due to the ability of NURBS to exactly represent circular geometries, the problem geometry was represented exactly, without approximation, at all levels of the discretization. Very good accuracy of all statistical data reported was achieved for this test case, even on very coarse meshes. The results rapidly converged to the DNS, while producing good quality solutions on coarser grids.

The proposed methodology builds on the weak formulation of the Navier–Stokes equations, and turbulence modeling does not make explicit use of eddy viscosities. We believe that this in part explains the good numerical performance of the proposed methodology on this particular problem. The turbulent Taylor–Couette flow is dominated by high rotation rates of the fluid, which cause problems for many well-accepted eddy-viscosity models (see [47]).

An important contribution of this paper is that the RBVMS formulation was shown to globally conserve angular momentum. This is in contrast to stabilized formulations of fluid flow that are otherwise very similar to the RBVMS formulation.

Acknowledgments

We would like to thank Prof. Steven Dong for providing us with the DNS data and Prof. Thomas J.R. Hughes for valuable discussions about rotating turbulent flows. We also wish to thank the Texas Advanced Computing Center (TACC) at the University of Texas at Austin for providing HPC resources that have contributed to the research results reported within this paper. Support of Teragrid Grant No. MCAD7S032 is gratefully acknowledged.

Appendix. Definition of stabilization and penalty parameters

In this appendix we provide the definitions of the interior stabilization parameters τ_M and τ_C as well as the boundary penalty parameter τ_B. These definitions are applicable to finite elements and isogeometric analysis where individual element domains are constructed by means of the isoparametric mapping of a reference element. This mapping denoted by $\boldsymbol{x}(\boldsymbol{\xi}) : \widehat{K} \to K,\ \boldsymbol{x} = \{x_i\}_{i=1}^d$ are the coordinates of the spatial element K, and $\boldsymbol{\xi} = \{\xi_i\}_{i=1}^d$ are the coordinates of the reference element $\widehat{K}$. The jacobian of this mapping and its inverse are $\frac{\partial x_i}{\partial \xi_j}$ and $\frac{\partial \xi_i}{\partial x_j}$, respectively. The jacobian gives the element length scales employed in the definition of stabilization and penalty parameters.

Interior stabilization parameters τ_M and τ_C are defined as follows (see [3] for the original reference):

$$\tau_M = \left(\frac{4}{\Delta t^2} + u_i^h G_{ij} u_j^h + C^I \nu^2 G_{ij} G_{ij} \right)^{-1/2}, \tag{A.1}$$

and

$$\tau_C = (\tau_M G_{ii})^{-1}, \tag{A.2}$$

where

$$G_{ij} = \frac{\partial \xi_k}{\partial x_i} \frac{\partial \xi_k}{\partial x_j}. \tag{A.3}$$

In the above definitions, Δt is the time step size, C^I is a positive constant of the element-wise inverse estimate that is independent of the mesh size (see, e.g., [34]), and summation on repeated indices is assumed. In the simulations presented here, we take $C^I = 36$.

The boundary penalty parameter is defined as follows (see [8] for the original reference):

$$\tau_B = \frac{u^{*2}}{\|\boldsymbol{u}_\tau^h\|}, \tag{A.4}$$

where $\boldsymbol{u}_\tau^h$ is the wall tangential or slip velocity defined as $\boldsymbol{u}_\tau^h = \boldsymbol{u}^h - (\boldsymbol{u}^h \cdot \boldsymbol{n})\boldsymbol{u}^h$, $\boldsymbol{n}$ is the wall outward normal, and $\|\cdot\|$ denotes the Euclidean distance. In (A.4), u^* satisfies the following set of nonlinear equations:

$$y^+ = u^+ + e^{-\chi B}\left(e^{-\chi u^+} - 1 - \chi u^+ - \frac{(\chi u^+)^2}{2} - \frac{(\chi u^+)^3}{6} \right), \tag{A.5}$$

$$y^+ = \frac{y u^*}{\nu}, \tag{A.6}$$

$$u^+ = \frac{\|\boldsymbol{u}_\tau^h\|}{u^*}, \tag{A.7}$$

and has the interpretation of friction velocity. The first equation is the well-known parameterization of the turbulent boundary layer known as Spalding's law-of-the-wall [46], where $\chi = 0.4,\ B = 5.5,\ y^+$ and u^+ are the non-dimensional distance from the wall and mean fluid speed, respectively, and $\nu = \mu/\rho$ is the kinematic viscosity. y is the vertical distance from the wall taken as a fraction of the element length in the wall-normal direction, that is,

$$y = \frac{h_b}{C_b^I}, \tag{A.8}$$

$$h_b = 2(n_i G_{ij} n_j)^{-1/2}, \tag{A.9}$$

where the second equation gives the wall-normal element mesh size. It can be shown from the above equations that if the wall-normal mesh size is such that the first element is contained within the viscous sublayer, τ_B simply becomes

$$\tau_B = \frac{\nu C_b^I}{h_b}. \tag{A.10}$$

This is a purely numerical definition, originally given in [6]. C_b^I is a positive constant of the element boundary inverse estimate, that is also independent of the mesh size. We take $C_b^I = 4$ in the simulations.

References

[1] I. Akkerman, Y. Bazilevs, V.M. Calo, T.J.R. Hughes, S. Hulshoff, The role of continuity in residual-based variational multiscale modeling of turbulence, Computational Mechanics 41 (2008) 371–378.

[2] D.N. Arnold, F. Brezzi, B. Cockburn, L.D. Marini, Unified analysis of discontinuous Galerkin methods for elliptic problems, SIAM Journal of Numerical Analysis 39 (2002) 1749–1779.

[3] Y. Bazilevs, V.M. Calo, J.A. Cottrel, T.J.R. Hughes, A. Reali, G. Scovazzi, Variational multiscale residual-based turbulence modeling for large eddy simulation of incompressible flows, Computer Methods in Applied Mechanics and Engineering 197 (2007) 173–201.
[4] Y. Bazilevs, V.M. Calo, T.J.R. Hughes, Y. Zhang, Isogeometric fluid–structure interaction: theory, algorithms, and computations, Computational Mechanics 43 (2008) 3–37.
[5] Y. Bazilevs, L. Beirao da Veiga, J.A. Cottrell, T.J.R. Hughes, G. Sangalli, Isogeometric analysis: approximation stability, and error estimates for *h*-refined meshes, Mathematical Models and Methods in Applied Sciences 16 (2006) 1031–1090.
[6] Y. Bazilevs, T.J.R. Hughes, Weak imposition of Dirichlet boundary conditions in fluid mechanics, Computers and Fluids 36 (2007) 12–26.
[7] Y. Bazilevs, T.J.R. Hughes, NURBS-based isogeometric analysis for the computation of flows about rotating components, Computational Mechanics 43 (2008) 143–150.
[8] Y. Bazilevs, C. Michler, V.M. Calo, T.J.R. Hughes, Weak Dirichlet boundary conditions for wall-bounded turbulent flows, Computer Methods in Applied Mechanics and Engineering 196 (2007) 4853–4862.
[9] Y. Bazilevs, C. Michler, V.M. Calo, T.J.R. Hughes, Isogeometric variational multiscale modeling of wall-bounded turbulent flows with weakly-enforced boundary conditions on unstretched meshes, Computer Methods in Applied Mechanics and Engineering 199 (2010) 780–790.
[10] M. Bilson, K. Bremhorst, Direct numerical simulation of turbulent Taylor–Couette flow, Journal of Fluid Mechanics 579 (2007) 227–270.
[11] A.N. Brooks, T.J.R. Hughes, Streamline upwind/Petrov–Galerkin formulations for convection dominated flows with particular emphasis on the incompressible Navier–Stokes equations, Computer Methods in Applied Mechanics and Engineering 32 (1982) 199–259.
[12] V.M. Calo, Residual-based Multiscale Turbulence Modeling: Finite Volume Simulation of Bypass Transition, Ph.D. Thesis, Department of Civil and Environmental Engineering, Stanford University, 2004.
[13] J. Chung, G.M. Hulbert, A time integration algorithm for structural dynamics with improved numerical dissipation: the generalized-α method, Journal of Applied Mechanics 60 (1993) 371–375.
[14] J.A. Cottrell, T.J.R. Hughes, Y. Bazilevs, Isogeometric Analysis: Toward Integration of CAD and FEA, Wiley, Chichester, 2009.
[15] S. Dong, DNS of turbulent Taylor–Couette flow, Journal of Fluid Mechanics 587 (2007) 373–393.
[16] S. Dong, Turbulent flow between counter-rotating concentric cylinders: a DNS study, Journal of Fluid Mechanics 615 (2008) 371–399.
[17] J.A. Evans, Y. Bazilevs, I. Babuška, T.J.R. Hughes, *N*-widths sup–infs and optimality ratios for the *k*-version of the isogeometric finite element method, Computer Methods in Applied Mechanics and Engineering 198 (2009) 1726–1741.
[18] G.E. Farin, NURBS Curves and Surfaces: From Projective Geometry to Practical Use, A.K. Peters, Ltd., Natick, MA, 1995.
[19] L.P. Franca, S. Frey, Stabilized finite element methods: II. The incompressible Navier–Stokes equations, Computer Methods in Applied Mechanics and Engineering 99 (1992) 209–233.
[20] H. Gomez, V.M. Calo, Y. Bazilevs, T.J.R. Hughes, Isogeometric analysis of the Cahn–Hilliard phase-field model, Computer Methods in Applied Mechanics and Engineering 197 (2008) 4333–4352.
[21] J. Holmen, T.J.R. Hughes, A.A. Oberai, G.N. Wells, Sensitivity of the scale partition for variational multiscale LES of channel flow, Physics of Fluids 16 (2004) 824–827.
[22] T.J.R. Hughes, Multiscale phenomena: Green's functions, the Dirichlet-to-Neumann formulation subgrid scale models, bubbles and the origins of stabilized methods, Computer Methods in Applied Mechanics and Engineering 127 (1995) 387–401.
[23] T.J.R. Hughes, G. Feijóo, L. Mazzei, J.B. Quincy, The variational multiscale method – a paradigm for computational mechanics, Computer Methods in Applied Mechanics and Engineering 166 (1998) 3–24.
[24] T.J.R. Hughes, V.M. Calo, G. Scovazzi, Variational and multiscale methods in turbulence, in: W. Gutkowski, T.A. Kowalewski (Eds.), Proceedings of the XXI International Congress of Theoretical and Applied Mechanics (IUTAM), Kluwer, 2004.
[25] T.J.R. Hughes, J.A. Cottrell, Y. Bazilevs, Isogeometric analysis: CAD, finite elements, NURBS, exact geometry, and mesh refinement, Computer Methods in Applied Mechanics and Engineering 194 (2005) 4135–4195.
[26] T.J.R. Hughes, L. Mazzei, K.E. Jansen, Large-eddy simulation and the variational multiscale method, Computing and Visualization in Science 3 (2000) 47–59.
[27] T.J.R. Hughes, L. Mazzei, A.A. Oberai, A.A. Wray, The multiscale formulation of large eddy simulation: decay of homogenous isotropic turbulence, Physics of Fluids 13 (2001) 505–512.
[28] T.J.R. Hughes, A.A. Oberai, L. Mazzei, Large-eddy simulation of turbulent channel flows by the variational multiscale method, Physics of Fluids 13 (2001) 1784–1799.
[29] T.J.R. Hughes, G. Sangalli, Variational multiscale analysis: the fine-scale Green's function, projection, optimization, localization, and stabilized methods, SIAM Journal of Numerical Analysis 45 (2007) 539–557.
[30] T.J.R. Hughes, G. Scovazzi, L.P. Franca, Multiscale and stabilized methods, in: E. Stein, R. de Borst, T.J.R. Hughes (Eds.), Encyclopedia of Computational Mechanics, Computational Fluid Dynamics, vol. 3, Wiley, 2004. Chapter 2.
[31] T.J. R Hughes, T.E. Tezduyar, Finite element methods for first-order hyperbolic systems with particular emphasis on the compressible Euler equations, Computer Methods in Applied Mechanics and Engineering 45 (1984) 217–284.
[32] T.J.R. Hughes, G.N. Wells, A.A. Wray, Energy transfers and spectral eddy viscosity of homogeneous isotropic turbulence: comparison of dynamic Smagorinsky and multiscale models over a range of discretizations, Physics of Fluids 16 (2004) 4044–4052.
[33] K.E. Jansen, C.H. Whiting, G.M. Hulbert, A generalized-α method for integrating the filtered Navier–Stokes equations with a stabilized finite element method, Computer Methods in Applied Mechanics and Engineering 190 (1999) 305–319.
[34] C. Johnson, Numerical Solution of Partial Differential Equations by the Finite Element Method, Cambridge University Press, Sweden, 1987.
[35] R.M. Kirby, G.E. Karniadakis, Spectral element and hp methods, in: E. Stein, R. de Borst, T.J.R. Hughes (Eds.), Encyclopedia of Computational Mechanics, Computational Fluid Dynamics, vol. 3, Wiley, 2004.
[36] A.G. Kravchenko, P. Moin, R. Moser, Zonal embedded grids for numerical simulation of wall-bounded turbulent flows, Journal of Computational Physics 127 (1996) 412–423.
[37] A.G. Kravchenko, P. Moin, K. Shariff, B-spline method and zonal grids for simulation of complex turbulent flows, Journal of Computational Physics 151 (1999) 757–789.
[38] W.Y. Kwok, R.D. Moser, J. Jiménez, A critical evaluation of the resolution properties of B-spline and compact finite difference methods, Journal of Computational Physics 174 (2001) 510–551.
[39] G. Lewis, H. Swinney, Velocity structure functions, scaling and transitions in high-Reynolds-number Couette–Taylor flow, Phys. Rev. E 59 (1999) 5457–5467.
[40] R.D. Moser, P. Moin, A. Leonard, A spectral numerical method for the Navier–Stokes equations with applications to Taylor–Couette flow, Journal of Computational Physics 52 (1983) 524–544.
[41] J. Nitsche, Uber ein variationsprinzip zur losung von Dirichlet-problemen bei verwendung von teilraumen, die keinen randbedingungen unterworfen sind, Abhandlungen aus dem Mathematischen Seminar der Universitat Hamburg 36 (1971) 9–15.
[42] P. Orlandi, D. Ebstein, Turbulent budgets in rotating pipes by DNS, International Journal of Heat and Fluid Flow 21 (2000) 499–505.
[43] L. Piegl, W. Tiller, The NURBS Book, Monographs in Visual Communication, second ed., Springer-Verlag, New York, 1997.
[44] D. Pirro, M. Quadrio, Direct numerical simulation of turbulent Taylor–Couette flow, European Journal of Mechanics – B/Fluids 27 (2007) 552–566.
[45] K. Shariff, R.D. Moser, Two-dimensional mesh embedding for B-spline methods, Journal of Computational Physics 145 (1998) 471–488.
[46] D.B. Spalding, A single formula for the law of the wall, Journal of Applied Mechanics 28 (1961) 444–458.
[47] C.G. Speziale, B.A. Younis, R. Rubinstein, Y. Zhou, On consistency conditions for rotating turbulent flows, Physics of Fluids 10 (1998) 2108–2110.
[48] T. Tezduyar, S. Aliabadi, M. Behr, A. Johnson, S. Mittal, Parallel finite element computation of 3D flows, Computer 26 (1993) 27–36.

[49] T.E. Tezduyar, Computation of moving boundaries and interfaces and stabilization parameters, International Journal of Numerical Methods in Fluids 43 (2003) 555–575.
[50] T.E. Tezduyar, S.K. Aliabadi, M. Behr, S. Mittal, Massively parallel finite element simulation of compressible and incompressible flows, Computer Methods in Applied Mechanics and Engineering 119 (1994) 157–177.
[51] J.A. Vastano, R.D. Moser, Short-time Lyapunov exponent analysis and the transition to chaos in Taylor–Couette flow, Journal of Fluid Mechanics 233 (1991) 83–118.